Available online at www.sciencedirect.com

ScienceDirect

Advances in Space Research 73 (2024) 5665–5679

ADVANCES IN SPACE RESEARCH (a COSPAR publication)

www.elsevier.com/locate/asr

High performance lunar constellation for navigation services to Moon orbiting users

Giovanni Zanotti *, Michele Ceresoli, Andrea Pasquale, Jacopo Prinetto, Michèle Lavagna

Politecnico di Milano - Aerospace Science and Technology Department, Via G. La Masa, 34, Milano 20156, Italy

Received 6 October 2022; received in revised form 14 March 2023; accepted 19 March 2023
Available online 24 March 2023

Abstract

In order to assist the ever growing number of missions planned to visit the Moon, an international effort is being made to design and commission a communication and navigation lunar constellation of satellites. To this purpose, the goal of this study is to provide first a strategy to help the design of a small-sized lunar constellation, entailing different objectives and users to assist. Then, various optimised constellations are tested including the orbital users' filtering architectures, extracting insights on the state estimation achievable and its capability to support critical GNC tasks.

Given the early stage design phase in which this study is carried out, the constellation design does not entail strong and clearly defined requirements yet. For such reason, a multi-objective optimisation (MOO) has been employed, which proved to be extremely beneficial, ensuring a correct amount of versatility to provide a large set of Pareto-optimal solutions. Different objectives associated to both various services and users have been put in place, exploring a search space based on classical Keplerian elements of the constellation servicers.

To compare the resulting constellations and validate correctly the performance from a navigation perspective the users navigation scheme has been considered to be based on a GNSS/INS tightly coupled formulation. The GNSS receiver measurements are fused with accelerometer outputs through a navigation filter, providing thus a strategy where the absence of GNSS observables is partially covered by an inertial propagation of the on-board state. Attention is here focused on polar orbiters operational in Low Lunar Orbit (LLO) environment and the obtained results showed navigation capabilities good enough to enable correct execution of missions in the low lunar orbital region.

Keywords: Moon; Constellation; Autonomous navigation; GNSS/INS coupling; Multi-objective optimisation

1. Introduction

For the next decades, it is clear that the lunar environment, given the continuous and renewed enthusiasm in this scenario, will be interested by many different missions that will explore the surface, with particular attention to surface assets such as landers, rovers and even humans (Laurini et al., 2010). Moreover, due to some specific features of the orography and mineralogy, the South Pole region will be for certain one of the most targeted spots on the surface (Wilhelms et al., 1979; Jessica Flahaut et al., 2020).

With this perspective in mind, the possibility of exploiting communication and navigation infrastructures on the Moon surface would be revolutionary for the enabling of specific exploration activities that require real-time operations from the Earth and precise positioning on-board. The objective of pushing towards spacecraft autonomy is certainly a key point to unlock the exploitation of more intelligent and adaptive platforms, which, related to the tendency to move more and more towards distributed and smaller systems, needs to be deeply investigated. In

* Corresponding author.
E-mail address: giovanni.zanotti@polimi.it (G. Zanotti).

https://doi.org/10.1016/j.asr.2023.03.032
0273-1177/

particular providing good Earth-independent navigation functions to the orbital users or to a lander is one of the major challenges nowadays and a long-term objective of several space agencies. Indeed, both ESA and NASA foresee the implementation of these dedicated systems to support the next generation of public and commercial Lunar exploration missions, targeting an initial deployment at the end of this decade (ESA, 2021; Israel et al., 2020). This infrastructure could then enable users to meet the strict requirements identified by the International Space Exploration Coordination Group (ISECG) to safely operate on the Lunar surface, such as landing within a 90 meters 3-sigma uncertainty from the targeted location (ISECG, 2019).

The importance of autonomy from ground-based operations is a relevant aspect, that could enable many different applications that require real-time Guidance, Navigation and Control (GNC) capabilities not possible with standard operators-in-the-loop strategies. Different techniques to deal with a completely autonomous GNC loop have been proposed in the literature, e.g. for rendez-vous scenarios (Colagrossi et al., 2021; Ceresoli et al., 2021), formation flying (Capannolo and Lavagna, 2022; Capannolo et al., 2023) or lunar landing (Silvestrini et al., 2022a; Silvestrini et al., 2022b; Lunghi et al., 2022). In all the previous cases a high level of autonomy is presented as feasible and effective, exploiting, for the navigation purposes, limited sensor suites based on visual information. However in all those scenarios, the navigation is achieved in a relative reference, with respect to some specific features recognised on the target spacecraft (for rendez-vous or formation flying) or on the lunar surface (for the landing cases). These approaches are extremely powerful, but can only be applied during the terminal phase, in close proximity. The work presented in this paper focuses on providing the navigation capability autonomously from ground-based operations for the preliminary phases, where the chasing spacecraft is not yet able to acquire relative measurements and requires a Moon-relative state estimation, specifically for the low altitude orbital regimes.

The approach chosen for the constellation design is to go for a complete multi-objective optimisation (MOO, (Stadler, 1988)), which will provide an overall flexibility that can be extremely beneficial for early phase mission analyses. Indeed, during the phase 0/A of the mission design, only some high-level requirements are typically available, which provide only broad goals. As such, providing a specific and targeted objective function is not always feasible, for which reason having the possibility to track multiple objectives is useful, also to help the process of framing the problem itself, exploring the vast research space and understanding, as a consequence, the boundary of feasibility.

In this specific framework, the basic goal is to provide an as complete as possible service of communication and navigation to a set of different lunar users, both on the surface and in orbit. In Pasquale et al. (2022a) we have shown how useful an MOO approach can be in different scenarios, targeting good performance and constraint satisfaction to a broad class of users located in different regions on the Moon surface, defined by latitude. The great interest concerning the South Pole of the Moon, considering the big number of planned lunar missions landing on this specific region, provides a good reason to explore more the performance of these possible users. Specifically, autonomous lunar landing is a challenging task, that requires very good navigation performance during its short but critical execution.

What our previous paper (Pasquale et al., 2022a) was not particularly looking at, is the performance of the constellation obtained with orbital users, which is instead the main target of this article. The additional complexity associated in computing the navigation performance of orbital users is given by the fact that the various Dilution Of Precision (DOP) indices are not sufficient in this case to give a complete overview of the scenario. Indeed orbital users, specifically landers, are very likely to be equipped with a wide sensor suite, in order to provide on-board state estimation through specific sensor fusion algorithms, i.e. navigation filters. The objective of this study is thus to develop the navigation scheme used by generic potential orbital users to exploit robustly and at the most the GNSS services provided by the lunar constellation.

Among the different orbital users that may be considered for this assessment, the Low Lunar Orbits (LLO) have been selected, i.e. circular orbits in the 50–150km altitude range. In the context of the Moon exploration roadmap, such orbits are foreseen to be used for many different reasons and by many missions. In addition, connected to the importance of the South Pole and the associated landers, polar LLOs are targeted in this work.

In this research work we present a complete framework for performing an MOO whose outputs are presented in the form of Pareto fronts, from which some best fit candidates are used as test case to simulate the proposed navigation filter and sensor fusion strategy.

After this brief introduction, the paper will go through the presentation of the optimisation setup in Section 2, passing through the definition of the various objectives and the related cost function evaluation processes. Then in Section 3 we present the complete navigation filter strategy and the ground truth model used for performance assessment. Section 4 will present first the MOO results and the results picking procedure, then the navigation performance simulation results. Finally in Section 5 we draw some conclusions and set the path for future work.

2. Optimisation setup

In order to perform an optimisation of the constellation with the goal of maximising the performance of the provided service, simulating the servicer-user interaction is a key element. In the following sub-sections we present the

key performance indices used to construct the cost function of the MOO.

2.1. Visibility

Consider the relative geometry of a satellite constellation element S_i and a user U_j on a different orbit. For simplicity, let's consider the planar case to illustrate the concepts associated to the reciprocal visibility between the satellites, whose geometry is illustrated in Fig. 1. First the point-to-point visibility between the two elements can be computed considering that, given the Moon-centric position of S_i and U_j as $\mathbf{r}_S, \mathbf{r}_U$ respectively, the relative position vector may be computed as:

$$\Delta\mathbf{r} = \mathbf{r}_S - \mathbf{r}_U \tag{1}$$

Therefore, the point-to-point visibility is achieved if $\Delta\mathbf{r}$ does not intersect the Moon, i.e., based on the approach proposed in Curtis (2013), analysing the values of the following angles, where the the radius $R_\mathbb{D}$ of the occulting spherical body is used.

$$\theta_{ij}(t) = \arccos \frac{\mathbf{r}_U(t) \cdot \mathbf{r}_S(t)}{\|\mathbf{r}_U(t)\| \|\mathbf{r}_S(t)\|} \tag{2}$$

$$\theta_i(t) = \arccos\left(R_\mathbb{D} / \|\mathbf{r}_S(t)\|\right) \tag{3}$$

$$\theta_j(t) = \arccos\left(R_\mathbb{D} / \|\mathbf{r}_U(t)\|\right) \tag{4}$$

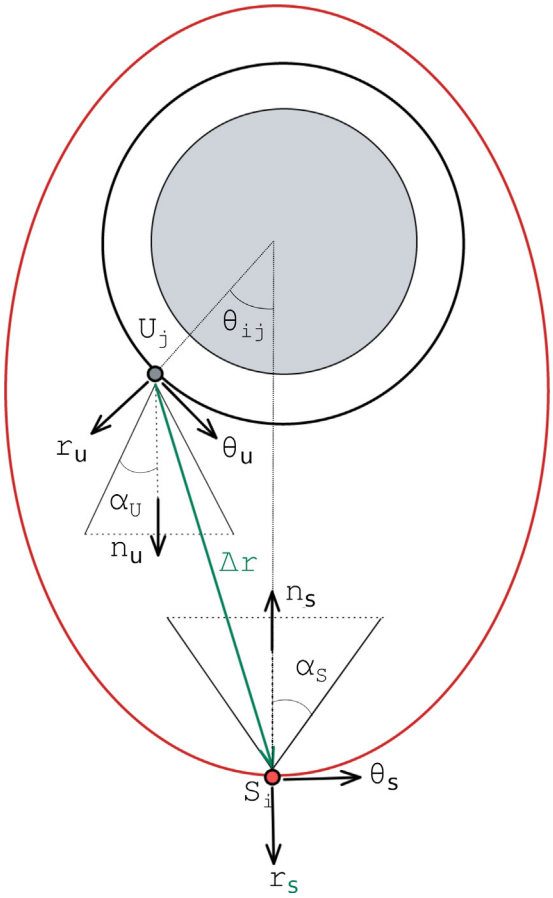

Fig. 1. User-servicer relative geometry.

Thus $\mathcal{V}^p_{ij}(t)$, the point-to-point (hence the superscript p) visibility function from the i-th satellite to the j-th user, can be defined by:

$$\mathcal{V}^p_{ij}(t) = \begin{cases} 0 & \text{if} \quad \theta_i(t) + \theta_i(t) \leqslant \theta_{ij}(t) \\ 1 & \text{elsewhere} \end{cases} \tag{5}$$

Then a Field-of-View (FoV) is associated to both the user and the servicers. In general, these could be oriented in any direction in the Local Vertical Local Horizon frame. Then, it is assumed that the pointing direction is represented by means of a direction vector $\mathbf{n}_U$ and $\mathbf{n}_S$ for the user and the servicer respectively, as well as each spacecraft has a circular FoV with half-cone angle α_U and α_S. The user and servicer FoV conditions, $\mathcal{V}_{\alpha,U}$ and $\mathcal{V}_{\alpha,S}$ respectively are defined as in Eqs 6 and 7.

$$\mathcal{V}_{\alpha,U}(t) = \begin{cases} 1 & \text{if} \quad \arccos \frac{\mathbf{n}_U(t) \cdot \Delta\mathbf{r}(t)}{\|\Delta\mathbf{r}(t)\|} < \alpha_U \\ 0 & \text{elsewhere} \end{cases} \tag{6}$$

$$\mathcal{V}_{\alpha,S}(t) = \begin{cases} 1 & \text{if} \quad \arccos \frac{\mathbf{n}_S(t) \cdot \Delta\mathbf{r}(t)}{\|\Delta\mathbf{r}(t)\|} < \alpha_S \\ 0 & \text{elsewhere} \end{cases} \tag{7}$$

Therefore the visibility between the servicer i and the user j can be computed as:

$$\mathcal{V}_{i,j}(t) = \begin{cases} 1 & \text{if} \quad \mathcal{V}^p_{ij}(t) \cdot \mathcal{V}_{\alpha,U}(t) \cdot \mathcal{V}_{\alpha,S}(t) = 1 \\ 0 & \text{elsewhere} \end{cases} \tag{8}$$

In case the coverage function of a j-th point is computed with respect to the whole satellite constellation, the satellite visibility functions $\mathcal{V}_{i,j}(t)$ of the constellation must be combined (Pasquale et al., 2022a). In particular, having defined the multi-sat coverage function, $\mathcal{N}_j(t)$:

$$\mathcal{N}_j(t) = \sum_i^N \mathcal{V}_{i,j}(t) \quad \text{s.t.} \quad \mathcal{N}_j : \mathbb{R} \to \mathbb{N} \tag{9}$$

the *n-fold continuous coverage index* can be defined as:

$$\mathcal{F}_j(t,n) = \begin{cases} 1 & \text{if} \quad \mathcal{N}_j(t) \geqslant n \\ 0 & \text{if} \quad \mathcal{N}_j(t) < n \end{cases} \tag{10}$$

2.2. Dilution of precision

The concept of DOP reflects the idea that the position error that results from measurement errors depends on the user relative geometry. The DOP figures therefore represent a key parameter for the evaluation of satellite constellation's navigation performance. The formal derivation of the DOP relations begins with the linearisation of the pseudorange equation (Kaplan and Hegarty, 2017). This linearisation provides the Jacobian $\mathbf{\Pi} \in \mathbb{R}^{n\times 4}$, which relates changes in the user position and time bias to changes in the pseudorange values. If this relationship is inverted, it can be used to relate the covariance of the user position and time bias to the covariance of the pseudorange errors.

$$\Delta \mathbf{x} = \mathbf{\Gamma}\,\Delta\boldsymbol{\rho} \quad \text{with} \begin{cases} \mathbf{\Gamma} = \mathbf{\Pi}^{-1} \text{ if } n = 4 \\ \mathbf{\Gamma} = \left(\mathbf{\Pi}^{\top}\mathbf{\Pi}\right)^{-1}\mathbf{\Pi}^{\top} \text{ elsewhere} \end{cases} \tag{11}$$

The DOP parameters then are defined as geometry factors that relate parameters of the user position and time bias errors to those of the pseudorange errors. The components of the matrix $\mathbf{\Theta} = \left(\mathbf{\Pi}^{\top}\mathbf{\Pi}\right)^{-1}$ quantify how pseudorange errors translate into components of the covariance of $\Delta\mathbf{x}$. The different DOP measures can be defined exploiting the different components of $\mathbf{\Theta}$, as per Eqs (12)–(16) indicating *geometric*, *position*, *horizontal*, *vertical* and *time* DOP respectively.

$$\texttt{GDOP} = \sqrt{\mathbf{\Theta}_{11} + \mathbf{\Theta}_{22} + \mathbf{\Theta}_{33} + \mathbf{\Theta}_{44}} \tag{12}$$

$$\texttt{PDOP} = \sqrt{\mathbf{\Theta}_{11} + \mathbf{\Theta}_{22} + \mathbf{\Theta}_{33}} \tag{13}$$

$$\texttt{HDOP} = \sqrt{\mathbf{\Theta}_{11} + \mathbf{\Theta}_{22}} \tag{14}$$

$$\texttt{VDOP} = \sqrt{\mathbf{\Theta}_{33}} \tag{15}$$

$$\texttt{TDOP} = \sqrt{\mathbf{\Theta}_{44}} \tag{16}$$

If only 3 satellites are in view, it is possible to assume that the vertical component is known a priori (e.g. for a surface user this is given by the local topography) and compute the horizontal component of the DOP only, namely the 2DHDOP. This is done by removing the third column (associated to the z-direction) from the $\mathbf{\Pi}$ matrix.

Moreover, in this study are considered of interest also the following quantities:

- $\texttt{DOPAV}_j = \mathcal{F}_j(t, 4)$ is used to identify the regions where the GDOP exists, and then its value is computed with Eq. 12.
- $\texttt{2DHDOPAV}_j = \mathcal{F}_j(t, 3)$ is used to identify the regions where the 2DHDOP exists, and then its value is computed with Eq. 14 on the $\mathbf{\Pi}$ matrix with the third column eliminated.

2.3. Genotype

In order to ensure that the performance of the constellation of satellites satisfies the different requirements and provides thus a quality and reliable service, an MOO procedure is set-up in line with what was done in Pasquale et al. (2022a). Its genotype is built in such a way that a constellation with n Keplerian Orbits is constructed. In particular, the design variables space has been defined as:

- n: number of constellation elements, *fixed a priori*;
- Semi-major axis (sma), eccentricity (ecc), inclination (Inc.) and argument of pericenter (aop) are considered to be the same for the whole constellation element: the orbit semi-major axis is *fixed a priori* to 9750.7km, in order to ensure a period of 24hours. The argument of pericenter is fixed to 90° such that the aposelene lies above the South Pole, thus spending most of the orbital period in its neighbourhood. The orbits are constrained to be of the LFO (*Lunar Frozen Orbit*) class, in order to ensure a more stable behaviour and thus to reduce station keeping expenditure. As such the inclination is no more a degree of freedom, but it is fully defined as function of the other Keplerian elements, as $\texttt{inc} = f(\texttt{sma}, \texttt{ecc}, \texttt{aop})$.
- Right-Ascension of the Ascending Node (ran) and true anomaly (tan) are optimised for every i-th constellation element.

Hence, the design variables vector $\mathbf{x}$ is defined as:

$$\mathbf{x} = \left(\texttt{ecc}, \texttt{ran}_i, \texttt{tan}_i\right)^{\top} \quad i = 1, \ldots, n \tag{17}$$

with a total number of $2n + 1$ variables.

2.4. Objectives and cost function

In order to showcase the flexibility and versatility of the proposed constellation design strategy, three different optimisation paths have been followed, i.e. three different cost functions are used. In particular, it is assumed that the interest is associated to the Lunar South Pole (SP, latitude $< -75°$) as well as the Low-Lunar Orbit (LLO, as polar circular orbiter in the range of altitudes between 50 and 150km). Regarding the SP, the objectives identified to be minimised for the present study are:

- SP_COMM_CONT: Percentage of South Pole users for which an 8 h continuous window per day is not present for at least 99% of the time.
- SP_NAV_NCONT: Percentage of South Pole users for which a daily 5 h non-continuous time window with 2DHDOPAV is not present for at least 99% of the time.

Instead, regarding the LLO region, the following minimisation objectives are identified as of interest:

- 2DHDOP_NCONT: Percentage of LLO users for which a daily 2 h non-continuous time window with 2DHDOP < 10 is not present for at least 99% of the time.
- LLO_mu: maximum among the different LLO users of the average 2-fold blind windows duration, i.e. the duration of windows where less than 2 satellites are in view, expressed in minutes.
- LLO_sigma: maximum among the different LLO users of the standard deviation of the 2-fold blind windows duration, expressed in minutes.
- LLO_musigma: Product of the previous two objectives, expressed in minutes squared. This component is added to collapse the previous two elements into a single one. It provides a trade-off result between windows duration and their variance in time and allows to reduce the number of objectives of the optimisation, which results more efficient and effective.

- `LLO_cum`: maximum among the different LLO users of the cumulative sum of the 2-fold blind windows duration, expressed in minutes.

The different values used in the objectives definition have been selected as challenging thresholds that can be reasonably reached by a small-sized constellation, imposing 99% of time, ensuring that over the simulation timespan the requests were satisfied almost every day. The duration of the required daily windows decreases related to the complexity of achieving the specific service, i.e. from 8 hours for communication requiring only 1-fold visibility, down to 2 hours for LLO `2DHDOP` with specific performance. The minimum value of `2DHDOP` < 10 is defined as a minimum threshold below which navigation performances are considered to be acceptable. The threshold of 2-fold blind windows for the `LLO_mu` and `LLO_sigma` objectives has been set after preliminary simulations showed that with at least 2 servicers in visibility the navigation filter was able to recover convergence from a diverged state.

From the previous objectives three different cost functions are assembled, as in the following.

- `full`: cost function comprising both `SP` and `LLO` related objectives – `SP_COMM_CONT`, `SP_NAV_CONT`, `SP_NAV_NCONT`, `2DHDOP_NCONT`, `LLO_mu`, `LLO_sigma`.
- `llo_sgl`: cost function comprising only `LLO` related objectives – `2DHDOP_NCONT`, `LLO_musigma` and `LLO_cum`, on a set of LLO users on a single `ran` value equal to 0°.
- `llo_mlt`: same cost function as before but on a set of LLO users on `ran` values spanning the range 0–360°.

The exploration of the design variables space and the generation of the Pareto fronts for the optimisation runs are performed through the exploitation of a *Multi-Objective Hypervolume-Based Ant Colony Optimisation* (MHACO) algorithm (Acciarini et al., 2020). The ESA *pagmo* (Biscani and Izzo, 2020) optimisation package has been exploited for that purpose. MHACO is preferred over standard heuristic methods, such as the *Non-Dominated Sorting Particle Swarm Optimiser* (NSPSO) (Li, 2003) or the *Non-Dominated Sorting Genetic Algorithm* (NSGA-II) (Deb et al., 2002), since it is shown to be really competitive with those algorithms, exhibiting superior performance in large search space exploration.

After a preliminary analysis, a population of 100 elements and a maximum number of 150 generations are considered.

3. On-board navigation strategy

As mentioned above, an orbital user exploiting a GNSS constellation is characterised by an evolution that requires the exploitation of a dynamical tracking problem, which can be handled with a Bayesian filter. In particular, among the different estimation algorithms, the most reliable and effective to work within a complete GNC scheme is the Kalman Filter, together with all its different variations. Given the limited size of the constellation under study, the user will eventually lose visibility with any of the servicers and consequently will need a way to continue with a propagation of its own state. To do this, a reasonable dynamical model is required on-board which, together with an accelerometer, can be beneficial in providing an inertial navigation solution for the blind windows.

3.1. Ground truth dynamics

In order to validate the navigation strategy, a complete high-fidelity propagation of the LLO users is required, for both simulating the dynamic evolution in the complexity of the cislunar environment and generating a trajectory to be used as ground truth reference.

The dynamics with which the ground truth trajectory is generated comprises two separated contributions:

- Gravitational effects
- Solar Radiation Pressure (SRP) perturbation

To describe the motion of the spacecraft with a negligible mass with respect to some central body, $\mathcal{P}_k$ (the Moon in this case) accounting for multiple gravitational sources, the relative formulation of the Restricted N-Body Problem (RnBP) can be expressed as:

$$\ddot{\mathbf{r}}_{ki} = -\frac{\mu_k}{r_{ki}^3}\mathbf{r}_{ki} + \sum_{\substack{j=1 \\ j\neq i,k}}^{N} \mu_j \left(\frac{\mathbf{r}_{ij}}{r_{ij}^3} - \frac{\mathbf{r}_{kj}}{r_{kj}^3} \right) \tag{18}$$

where the motion of the spacecraft $\mathcal{P}_i$, with respect to the central body $\mathcal{P}_k$, under the gravitational influence of the point masses $\mathcal{P}_j$ is modelled.

If the relative position vector $\mathbf{r}_{kj}$, that represents the location of the j-th perturbing body with respect to the central body is obtained from high fidelity ephemerides, the RnBP is reduced to the Ephemeris Restricted N-Body Problem (ERnBP). In this work, NAIF's SPICE library (Acton, 1996) is exploited and DE440 ephemerides are used, whereas the relative position vector $\mathbf{r}_{ij}$ is computed by vector subtraction as:

$$\mathbf{r}_{ji} = \mathbf{r}_{kj} - \mathbf{r}_{ki} \tag{19}$$

and represents the location of the perturbing body $\mathcal{P}_j$ with respect to the object of interest, $\mathcal{P}_i$.

For the ground truth we accounted for a detailed full ephemerides model including Moon, Earth and Sun contributions. The contributions from the other solar system bodies have been deemed negligible in the LLO environment. What is instead much more relevant is the contribution of the irregular gravity field of the Moon, which is included with a spherical harmonics model, where the

attractor's shape is assumed to be representable through the use of spherical harmonic functions of increasing order. Although in practical application the series is truncated at a certain order, it is proven to converge to the real gravity field. The required inputs are the coefficients of the expansion and the mass. An overview of the method is found in Schaub and Junkins (2005, 2022b). The mathematical representation of the gravitational potential can be expressed as per Eq. 20.

$$\begin{aligned} U_{\text{she}} &= \frac{\mu}{r} + \frac{\mu}{r}\sum_{n=2}^{N}\sum_{m=0}^{n}\left(\frac{R_0}{r}\right)^n [C_{nm}\cos(m\lambda) \\ &\quad + S_{nm}\sin(m\lambda)]P_{nm}(\cos\theta) \end{aligned} \tag{20}$$

where μ is the gravitational parameter of the central body, r the distance to the center of mass of the body, λ the longitude, θ the co-latitude, R_0 a reference radius, $P_{nm}(x)$ are Associated Legendre Functions, while C_{nm} and S_{nm} are Stokes coefficients.

In this work, we considered the harmonics up to the 60th order, with the values of the coefficients derived from the LP165P model (Konopliv et al., 1998).

Regarding the SRP, the acceleration, directed in the anti-Sun direction, shows a magnitude that can be described as presented in Vallado (2001), as in Eq. 21.

$$a_{SRP} = \frac{S_\odot}{c}\frac{(1\text{AU})^2}{d_\odot^2} c_R \frac{A_\odot}{m} \tag{21}$$

In the latter, $S_\odot = 1367\text{Wm}^{-2}$ is the Sun mean flux at 1AU, $c = 299792458\text{ms}^{-1}$ the speed of light, $d_\odot$ the current Sun-body distance, c_R the reflectivity and $A_\odot$ the cross-sectional area of the body exposed to the radiation. Generic values of $c_R = 0.7$ and $m/A = 150\text{kgm}^{-2}$ have been assumed for this scenario, representative of a medium-sized spacecraft. This simplified *cannonball* model for SRP is useful since it avoids the dependence of orbital dynamics on the spacecraft attitude which would have coupled the system in a full 6-DOF dynamical state. In this way, it is not necessary to assume any peculiar pointing profile for the spacecraft and a detailed model for all the reflective surfaces of the platform is not needed.

3.2. Observables

Dealing with a navigation filter, it is fundamental to analyse correctly the measurements that are exploited by the estimation algorithm, in order to be capable to correctly simulate the behaviour of the sensors providing such observables and to find proper ways to define the measurement function used within the filter itself.

For this work, we considered a *One-Way* navigation solution, where the user terminal retrieves from any visible element of the constellation the range ρ, the range-rate $\dot{\rho}$, and the servicer ephemeris under the form of the state vector $\mathbf{x}_{s,i}$. When dealing with GNSS-related measurements, it is usual to define the observable data as *pseudorange* $\tilde{\rho}$ and *pseudorange-rate* $\tilde{\dot{\rho}}$, in order to indicate that the two measurements are affected by errors. In particular, looking at the range measurement, the geometric range obtained from the i^{th} servicer can be defined as per Eq. 21

$$\rho_i = c\Delta t_i = \|\mathbf{r}_{s,i} - \mathbf{r}\| \tag{22}$$

where c is the speed of light and Δt_i the time required for the signal to travel from the servicer position $\mathbf{r}_{s,i}$ to the user one $\mathbf{r}$. In a *One-Way* ranging, this time difference is obtained by subtracting the servicer clock-time at signal emission from the user clock-time at reception, i.e. $\Delta t_i = t_u - t_{s,i}$. The two clocks are however not measuring the exact time, but they will present some offsets, which will in general be different between themselves. As such the measured time difference from the user terminal will bring us to the pseudorange as per Eq. 23.

$$\tilde{\rho}_i = c\,(t_u + \delta t_u - t_{s,i} - \delta t_{s,i}) = \rho_i + c\delta t_u + \varepsilon_{\delta t_{s,i}} \tag{23}$$

From this equation, it is clear that a bias in the measurements can be present. In addition to that, there is a huge number of other possible sources of error in the pseudorange, due to RF interference effects, distortions of the signals both within the terminals or caused by interaction with the propagation medium, multipath losses, and also relativistic effects, leading to a final pseudorange formulation as per Eq. 24, where all the previous contributions (including $\varepsilon_{\delta t_{s,i}}$) are combined in a single component ε_ρ.

$$\tilde{\rho}_i = \rho_i + c\delta t_u + \varepsilon_\rho \tag{24}$$

The same kind of reasoning can be done for the pseudorange-rate observable, which can be derived directly from the observed frequency Doppler shift Δf_D, but again is inherently affected by the same effects as in the previous case, summed up in a $\varepsilon_{\dot{\rho}}$ term in addition to the time bias derivative.

$$\tilde{\dot{\rho}}_i = c\frac{\Delta f_D}{f_{s,i}} + c\dot{\delta t}_u + \varepsilon_{\dot{\rho}} \tag{25}$$

To enter the details of GNSS systems a good reference can be found in Kaplan and Hegarty (2017).

For this work, in order to simulate these effects, we implemented the model in Eqs 26 and 27 to generate the measurements fed to the filter.

$$\tilde{\rho}_i = \|\tilde{\mathbf{r}}_{s,i} - \mathbf{r}\| + b_c + \varepsilon_\rho \tag{26}$$

$$\tilde{\dot{\rho}}_i = (\tilde{\mathbf{v}}_{s,i} - \mathbf{v}) \cdot (\tilde{\mathbf{r}}_{s,i} - \mathbf{r})/\rho + d_c + \varepsilon_{\dot{\rho}} \tag{27}$$

$$\tilde{\mathbf{x}}_{s,i} = \left[\tilde{\mathbf{r}}_{s,i}^\top, \quad \tilde{\mathbf{v}}_{s,i}^\top\right]^\top = \mathbf{x}_{s,i} + \left[\boldsymbol{\varepsilon}_r^{1\times3}, \quad \boldsymbol{\varepsilon}_v^{1\times3}\right]^\top \tag{28}$$

For both the observables, all the effects are directly collected in single noisy gaussian terms, except for the receiver clock bias b_c and drift d_c contributions, which are treated as an additional parameter to be estimated. The standard deviations associated to ε_ρ and $\varepsilon_{\dot{\rho}}$ are $\sigma_\rho = 10\text{m}$ and $\sigma_{\dot{\rho}} = 0.1\text{ms}^{-1}$ (Giordano et al., 2021).

The receiver clock bias and drift, which represent $c\delta t_u$ and $c\dot{\delta} t_u$ respectively, are simulated with the dynamical model in Eqs 29 and 30:

$$\dot{b}_c = d_c + \varepsilon_{b_c} \tag{29}$$

$$\dot{d}_c = \varepsilon_{d_c} \tag{30}$$

where the stochastic components ε_{b_c} and ε_{d_c} are normally distributed with null mean and standard deviations of 100m and 1ms^{-1} (Grenier et al., 2022).

The servicers' ephemerides are affected by the related platforms navigation errors, which are added with a simple additive white gaussian noise model, as in Eq. 28, where $\boldsymbol{\varepsilon}_r^{1\times3}$ and $\boldsymbol{\varepsilon}_v^{1\times3}$ represent the three-dimensional position and velocity error vectors, defined by standard deviations of σ_r and σ_v.

Given that such ephemerides will be exploited to construct the on-board pseudorange and pseudorange-rate measurements within the filter, it is important to assess how the related uncertainties will propagate on such measurement. For this purpose the *Root of the Sum of the Squares* (RSS) principle is applied, for which the errors in pseudorange and pseudorange-rate derived from the ephemeris errors are given as per Eq. 31 and Eq. 32 respectively.

$$\sigma_{\rho_i,\mathbf{x}_{s,i}} = \left(\left[\left(\frac{\partial \rho_i}{\partial x_i}\right)^2 + \left(\frac{\partial \rho_i}{\partial y_i}\right)^2 + \left(\frac{\partial \rho_i}{\partial z_i}\right)^2 \right] \sigma_r^2 + \left[\left(\frac{\partial \rho_i}{\partial v_{xi}}\right)^2 + \left(\frac{\partial \rho_i}{\partial v_{yi}}\right)^2 + \left(\frac{\partial \rho_i}{\partial v_{zi}}\right)^2 \right] \sigma_v^2 \right)^{1/2} \tag{31}$$

$$\sigma_{\dot{\rho}_i,\mathbf{x}_{s,i}} = \left(\left[\left(\frac{\partial \dot{\rho}_i}{\partial x_i}\right)^2 + \left(\frac{\partial \dot{\rho}_i}{\partial y_i}\right)^2 + \left(\frac{\partial \dot{\rho}_i}{\partial z_i}\right)^2 \right] \sigma_r^2 + \left[\left(\frac{\partial \dot{\rho}_i}{\partial v_{xi}}\right)^2 + \left(\frac{\partial \dot{\rho}_i}{\partial v_{yi}}\right)^2 + \left(\frac{\partial \dot{\rho}_i}{\partial v_{zi}}\right)^2 \right] \sigma_v^2 \right)^{1/2} \tag{32}$$

Developing all the partial derivatives of range and range-rate, expressed as in Eqs 26 and 27, the mathematical expressions remain simple for the pseudorange, while they grow quite cumbersome for the pseudorange-rate. After the necessary simplifications, the resulting expressions are the following Eqs 33 and 34.

$$\sigma_{\rho_i,\mathbf{x}_{s,i}} = \sigma_r \tag{33}$$

$$\sigma_{\dot{\rho}_i,\mathbf{x}_{s,i}} = \left(\left[(v_x - v_{xi})^2 + (v_y - v_{yi})^2 + (v_z - v_{zi})^2 - \dot{\rho}_i^2 \right] \sigma_r^2/\rho_i^2 + \sigma_v^2 \right)^{1/2} = \sqrt{\alpha\sigma_r^2 + \sigma_v^2)} \tag{34}$$

It turns out that the position error is propagated exactly in the pseudorange when the uncertainty on the servicer ephemerides position is uniform among the three directions. Instead, for the pseudorange-rate, the effect of both ephemerides position and velocity uncertainties is present. Moreover the latter, due to the coefficient $\alpha = \alpha(\mathbf{v}, \mathbf{v}_{s,i})$ showing dependence on the current values of the velocity components for both user and servicers, cannot be used directly in this formulation. To avoid having an adaptive formulation, the expression of the coefficient α is evaluated a priori as the mean value experienced on the simulated trajectories of four different LLO users from 10 to 250km. The values of the ephemeris error standard deviation are $\sigma_r =$ 15m and $\sigma_v = 0.15\text{ms}^{-1}$, in line with the Galileo Service Definition Document (European Commission, 2019).

Concerning the accelerometers contained in the IMU, also in this case, it is fundamental to recall that such sensors are insensitive to volume-forces, such as all the gravitational effects included in the environment of our simulation. They are however sensitive to SRP, which in turn may be one of the most complex effects to correctly reproduce on board, for which reason an accelerometer can be extremely useful in this scenario.

It is possible to provide high-fidelity models to simulate its noisy measurements. In general it is possible to include biases, drifts, nonlinearities, misalignment and scale errors. For the purpose of this work, we decided to simplify the model, collecting all such effects into a single term. As a consequence, the simulated sensor reading is defined by the SRP contribution affected by an additive white gaussian noise, as per Eq. 35 with a standard deviation of $3.5 \times 10^{-4}\text{ms}^{-2}$, representative of standard high fidelity accelerometers (Northrop Grumman, 2022).

$$\tilde{\mathbf{a}}_{IMU} = \mathbf{a}_{SRP} + \varepsilon_{IMU} \tag{35}$$

3.3. Filter structure and implementation

Given the different nature of the measurements used, a suitable way to perform sensor fusion is needed, exploiting both the accelerometer, pseudorange and pseudorange-rate information. We faced this challenge through a tightly coupled GNSS/INS formulation, as described by the scheme in Fig. 2.

The acceleration $\tilde{\mathbf{a}}_{IMU}$ measured by the IMU is exploited in dynamical compensation mode (Crassidis and Junkins, 2011), added to the on-board dynamical model, to perform the state prediction step in the filter, outputing the a priori estimate $\hat{\mathbf{x}}_k^-$ at time step k. The GNSS observables of the pseudorange $\tilde{\rho}_i$ and pseudorange-rate $\tilde{\dot{\rho}}_i$ together with the ephemeris of each constellation satellite are instead passed as measurements directly to the filter, which, by performing

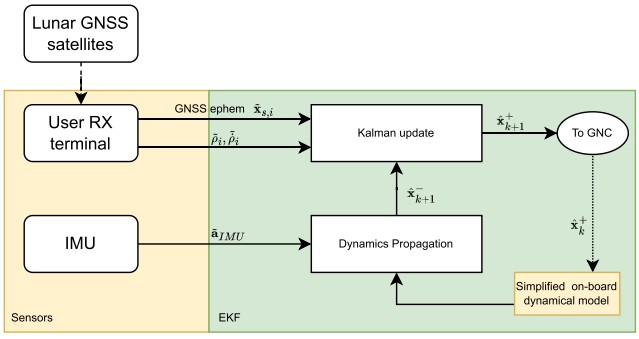

Fig. 2. Description of the GNSS/INS Navigation formulation.

the update step, returns the a posteriori corrected state $\hat{\mathbf{x}}_k^+$. The advantages of a *tightly coupled* GNSS/INS formulation over a *loosely coupled* one (Falco et al., 2017) where the GNSS receiver is considered as a black-box outputting the complete state directly reside in the possibility to exploit the GNSS signals also when less than 4 satellites are in visibility, which - for the proposed scenario - can be a very likely condition due to the limited number of constellation elements. Whenever no GNSS signal is available, the proposed architecture continues propagating on board the user position exploiting the information from the IMU only.

Given the choice to include also the clock bias b_c and drift d_c in the estimated parameters, the spacecraft state $\mathbf{x}_{S/C}$ is appended by these components, forming an overall filter state $\mathbf{x} = [\mathbf{x}_{S/C}^\top,\ b_c,\ d_c]^\top$.

The implemented filter is an Extended Kalman Filter, defined by the following simplified spacecraft dynamical model $\mathbf{f}_{S/C}(\mathbf{x}_{S/C}, \tilde{\mathbf{a}}_{IMU})$ and a clock dynamical model for the propagation and measurement function $\mathbf{h}(\mathbf{x}, \tilde{\mathbf{x}}_{s,i})$, defined as in Eqs 36 and 37.

$$\mathbf{f}_{S/C}(\mathbf{x}_{S/C}, \tilde{\mathbf{a}}_{IMU}) = \mathbf{f}_{S/C}(\mathbf{x}_{S/C})_{\mathfrak{D}} + \mathbf{f}_{S/C}(\mathbf{x}_{S/C})_{\mathfrak{F}} + \tilde{\mathbf{a}}_{IMU} \quad (36)$$

$$\mathbf{h}(\mathbf{x}, \tilde{\mathbf{x}}_{s,i}) = [\,\rho_1,\ \dot{\rho}_1,\ \rho_2,\ \dot{\rho}_2,\ \ldots,\ \rho_n,\ \dot{\rho}_n\,]^\top \quad (37)$$

From Eq. 36 it is possible to see the dynamic model replacement strategy to exploit the accelerometer in the navigation filter, including thus the SRP acceleration contributions. Moreover, the only gravitational terms inserted here are those associated to the Moon and Earth point mass gravitational potential. The Moon irregular mass distribution and the Sun gravity are not modelled here, in order to reduce the computational burden on the onboard computer. We want also to recall that the measurement function (Eq. 37) uses the estimated clock bias and drift to correct the pseudorange and range-rate a priori predictions, following Eqs 26 and 27. Associated to these parameters, their propagation model is instead given by $\mathbf{f}_c$ defined by Eq. 38.

$$\mathbf{f}_c = \begin{cases} \dot{b}_c &= d_c \\ \dot{d}_c &= 0 \end{cases} \quad (38)$$

Stacking then Eqs 36 and 38, we obtain the dynamical model to be used in the filter $\mathbf{f} = [\mathbf{f}_{S/C}^\top,\ \mathbf{f}_c^\top]^\top$. Algorithm 1 reports the most relevant steps of the EKF procedure in a pseudo-code format.

Algorithm 1. Extended Kalman Filter

$\hat{\mathbf{x}}_{k+1}^- = \int_{t_k}^{t_{k+1}} f(\mathbf{x}(\tau), \tilde{\mathbf{a}}_{IMU})d\tau, \quad \mathbf{x}_k = \hat{\mathbf{x}}_k^+, \quad \hat{\mathbf{x}}_0^+ = \hat{\mathbf{x}}_0$	▷ Absolute state propagation
$\mathbf{F}_k = \frac{\partial \mathbf{f}}{\partial \mathbf{x}}\big\|_{\hat{\mathbf{x}}_k^+}, \quad \mathbf{H}_{k+1} = \frac{\partial \mathbf{h}}{\partial \mathbf{x}}\big\|_{\hat{\mathbf{x}}_{k+1}^-}$	▷ State and measurement Jacobian matrices
$\mathbf{\Phi}(t_{k+1}, t_k) = \mathbf{I}_{6x6} + \mathbf{F}_k \Delta t$	▷ State Transition Matrix
$\mathbf{P}_{k^+1} - = \mathbf{\Phi}(t_{k+1}, t_k)\mathbf{P}_k^+ \mathbf{\Phi}^T(t_{k+1}, t_k) + \mathbf{Q}, \quad \mathbf{P}_0^+ = \mathbf{P}_0$	▷ State Covariance matrix propagation
$\mathbf{K}_{k+1} = \mathbf{P}_{k+1}^- \mathbf{H}_{k+1}^T (\mathbf{H}_{k+1}\mathbf{P}_{k+1}^- \mathbf{H}_{k+1}^T + \mathbf{R})^{-1}$	▷ Kalman gain matrix computation
$\hat{\mathbf{x}}_{k+1}^+ = \hat{\mathbf{x}}_{k+1}^- + \mathbf{K}_{k+1}(\tilde{\mathbf{y}}_{k+1} - h(\hat{\mathbf{x}}_{k+1}^-, \tilde{\mathbf{x}}_{s,i,k+1}))$	▷ State correction
$\mathbf{P}_{k+1}^+ = (\mathbf{I} - \mathbf{K}_{k+1}\mathbf{H}_{k+1})\mathbf{P}_{k+1}^- (\mathbf{I} - \mathbf{K}_{k+1}\mathbf{H}_{k+1})^T + \mathbf{K}_{k+1}\mathbf{R}\mathbf{K}_{k+1}^T$	▷ State Covariance matrix correction

The filter is here initialised with initial conditions of the state $\hat{\mathbf{x}}_0$ and the state covariance matrix $\mathbf{P}_0$, which are both set at the beginning of the simulation. We used $\sigma_{r,0} = 1\text{km}$ and $\sigma_{v,0} = 1\text{ms}^{-1}$ as values for $\mathbf{P}_0$ and as standard deviation for $\hat{\mathbf{x}}_0$. The process and measurement noise covariance matrices are represented by $\mathbf{Q}$ and $\mathbf{R}$ respectively. The former can be considered as a tuning parameter, the latter is instead defined by the sensors accuracy.

The evaluation of the innovation vector defined by $\tilde{\mathbf{y}}_{k+1} - h(\hat{\mathbf{x}}_{k+1}^-, \tilde{\mathbf{x}}_{s,i,k+1})$ is affected by two independent errors, i.e. the pseudorange and range-rate errors (introduced by the physics of the signals transmission and the RF terminals) and the error introduced in the servicers' ephemerides (given by the servicers' own navigation budget).

4. Results

Now we will go through the results obtained by the complete analysis, starting from the inspection of the optimisation results and the related extraction of the best candidate per each cost function. Then the simulation of the navigation filter will be carried out for some of the extracted candidates, in order to assess the performance and drive some conclusions on the explored strategy.

4.1. Pareto front analysis

As described in the previous sections the optimisation scheme presented is used to run three different objective functions, namely `full` accounting for both South Pole and LLO users performance, `llo_sgl` and `llo_mlt` considering instead only `LLO` related performance, both considering mean, standard deviation and cumulative sum of the 2-fold blind windows duration, the former for a single class of LLO users and the latter for a wider selection.

Moreover, each optimisation has been run letting the fixed parameter of the constellation size n vary between 4 and 6, leading to a number of three optimisation runs per each cost function. In the following we analyse the collection of the results in the form of Pareto plots, showing the population of the three constellation sizes in the cost function space per each objective function.

Fig. 3 shows the results for the objective function `full`. The associated cost function vector is six-dimensional, however in this plot we presented only the solutions that fully satisfy the South Pole related constraint per each user, i.e. those showing 0% for `SP_COMM_CONT`, `SP_NAV_CONT` and `SP_NAV_NCONT`. First from the top left and bottom left plots we highlight that the objective `2DHDOP_NCONT` being a percentage, it undergoes effects of saturation, for which reason a full Pareto front is not visible in those graphs. It is instead visible as a clearer front in the `LLO_sigma` vs `LLO_mu` plot. To extract the best solution, we favoured the different objectives in the following manner. First the solutions with the best values for `2DHDOP_NCONT` are selected, and among those only two Pareto optimal solutions are considered, minimising one of the two remaining objectives at a time. For the run with $n = 4$ no solution with `2DHDOP_NCONT` completely satisfied (i.e. 0%) is present, reaching a minimum value of 50% of the users. The best solutions taken from $n = 5$ and $n = 6$, satisfies instead this requirement completely.

The Pareto plot in Fig. 4 for the objective function `llo_sgl` is easier to read, since in this case only two objectives are displayed, comparing `LLO_cum` and `LLO_musigma`.

Indeed, in this case for all three constellation sizes, there are solutions with the `2DHDOP_NCONT` saturated to 0, so the extraction of the best candidate is simply done by picking 2 Pareto points favouring one of the two remaining objectives.

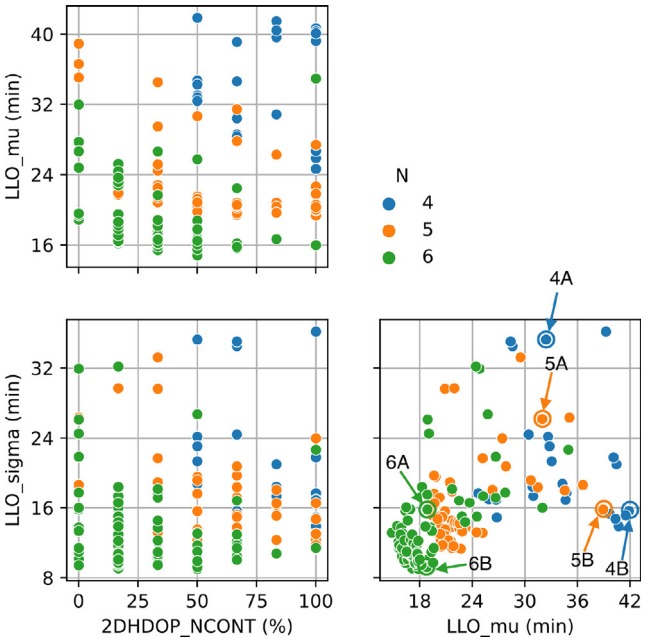

Fig. 3. Population optimised with the objective function `full`.

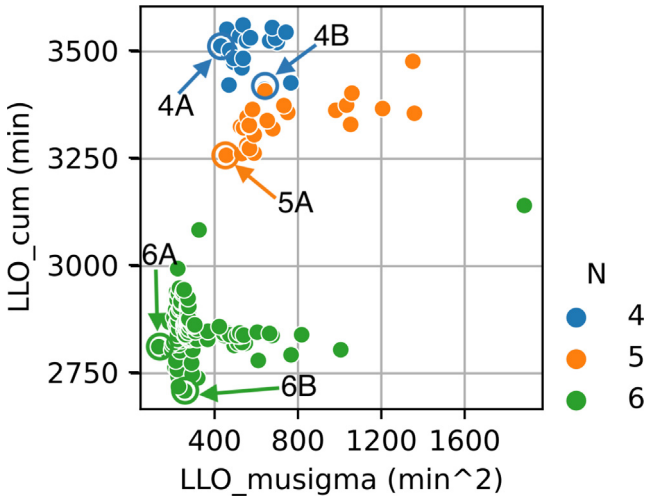

Fig. 4. Population optimised with the objective function `llo_sgl`.

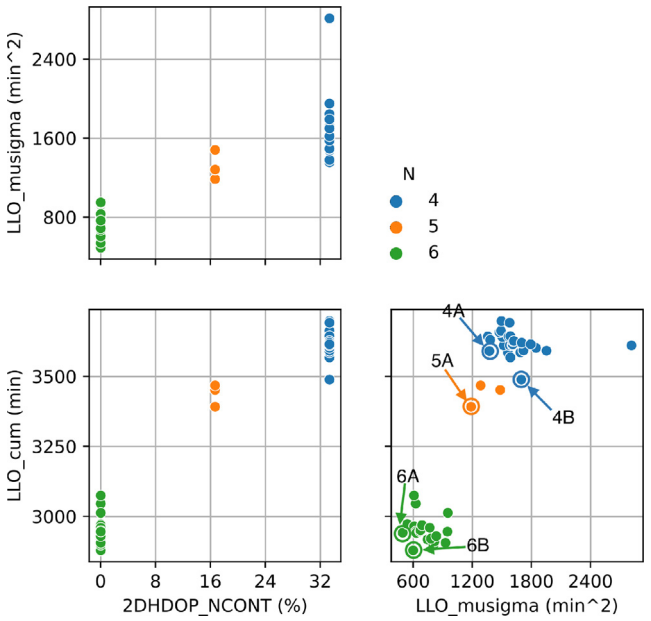

Fig. 5. Population optimised with the objective function `llo_mlt`.

Similar considerations apply also for the `llo_mlt`, whose solutions are presented in Fig. 5. In this case there are 0% `2DHDOP_NCONT` solutions only for $n = 6$, so the best solutions for $n = 4$ are picked among the 33.3% solutions, while those for $n = 5$ among the 16.7% solutions. Also here, two solutions optimal for the two remaining objectives are taken per each constellation.

After having collected these results from the Pareto plots, we can analyse the solutions, which are summarised in Table 1, where also the eccentricity `ecc` and the inclination `Inc.` are displayed. Recall that having constrained the orbit to be frozen, the latter is always a function of the former, providing no additional degree of freedom.

Table 1
Summary of the extracted results, per each objective function and per each constellation size. Column SP comprehends all the objectives associated to South Pole users.

Cost fcn	*ID*	ecc [-]	Inc. [°]	SP [%]	2DHDOP_NCONT [%]	LLO_mu [min]	LLO_sigma [min]	LLO_musigma [min^2]	LLO_cum [min]
full	4A	0.668	54.81	0%	50%	32	35	–	–
	4B	0.664	54.59	0%	50%	42	16	–	–
	5A	0.608	52.06	0%	0%	32	26	–	–
	5B	0.678	55.29	0%	0%	39	16	–	–
	6A	0.654	54.13	0%	0%	19	16	–	–
	6B	0.550	49.70	0%	0%	19	9	–	–
llo_sgl	4A	0.452	46.29	–	0%	–	–	430	3513
	4B	0.441	45.95	–	0%	–	–	640	3412
	5A	0.583	51.01	–	0%	–	–	456	3258
	6A	0.489	47.50	–	0%	–	–	132	2812
	6B	0.518	48.49	–	0%	–	–	256	2709
llo_mlt	4A	0.570	50.45	–	33.3%	–	–	1357	3643
	4B	0.548	49.60	–	33.3%	–	–	1696	3489
	5A	0.594	51.45	–	16.7%	–	–	1187	3392
	6A	0.556	49.93	–	0%	–	–	493	2942
	6B	0.649	53.90	–	0%	–	–	598	2879

Looking at the complete picture, it is possible to derive some relevant insights on the characteristics of the solutions. One of the first things that pops up is the evolution of the eccentricity value, that varies vastly from the first objective function full, where the upper boundary of 0.7 is almost reached, to the second one llo_sgl where the eccentricity reaches values lower than 0.5. This can be justified by the presence of the South Pole within the user regions for which performance shall be maximised. Having indeed higher eccentricities (recalling the imposed anomaly of pericenter of 90°) means spending more time around the aposelene, i.e. closer to the South Pole for the inclinations between 0° and 180°, enlarging the visibility duration. This value is generally decreasing for larger constellation sizes, due to the higher performance obtainable when increasing this parameter. In the third objective llo_mlt, instead, intermediate values of eccentricity are obtained, with the maximum value of 0.649 for the solution with $n = 6$.

After that, we can see that the objectives of the different solutions are always decreasing for increasing constellation size. This is expected as a general remark. It is also quite reasonable that worse values are obtained in the third objective llo_mlt with respect to what was obtained for the second one, which is optimised for a specific set of LLO users on a single orbital plane.

Fig. 6 displays the geometries of the obtained constellation for three different cases. In particular, the first two plots show the selected solutions of the optimisation with llo_sgl for case 5A (left) and 6A (center). From the solution with $n = 5$ we see basically three orbiters clustered on similar planes, while the remaining two are placed in separate planes covering the remaining space. The 6A solution presents instead a clear clustered solution, with only two planes considered, with their node axis aligned to the x-axis of the *LME2000* inertial frame. The optimality of this solution can be explained by recalling that the LLO users considered by the llo_sgl, having ran equal to 0, lie on the x-z plane. The DOP can thus be minimised by two clusters of servicers that are symmetric with respect to that orbital plane. With an odd number of satellites, the geom-

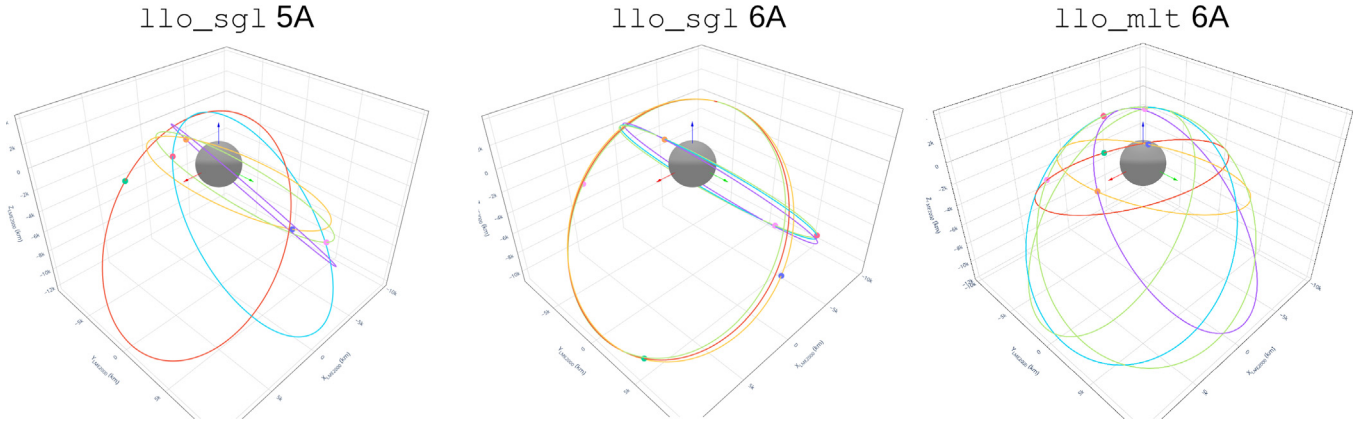

Fig. 6. Representation of three solutions extracted from the optimisation procedure for the cost functions llo_sgl and llo_mlt with $n = 5$ and $n = 6$.

etry becomes more complicated, nevertheless a similar effect is partly present also in the 5A constellation (left plot), where we can identify a cluster of three satellites with similar values of `ran` that is symmetric with respect to the x-z plane to the servicer on the red orbit. The remaining 5th servicer on the light-blue orbit lies, instead, between the former two.

This clustering is instead completely destroyed in the right plot, where the 6A solution for the `llo_mlt` cost function is displayed. Here, we see instead a different behaviour, where the 6 orbiters are displaced on almost 6 symmetric planes. This effect is clearly determined by the targetting of different orbital plane users, with `ran` spanning the whole 360° space.

4.2. Filter performance verification

In this additional step, a subset of the extracted solutions is analysed more in depth, verifying the proposed on-board navigation scheme in terms of performance, comparing the level of accuracy obtained in the state estimation and the duration of the convergence losses due to the 2-fold blind windows. The simulation is set up for a single polar LLO user with an altitude of 50 km, a `ran` of 0° (the same as the one of the users considered for the `llo_sgl` optimisation) and a total simulation time of 48 h.

Fig. 7 reports the zoomed simulation outcomes for the specific case of $n = 4$ in the optimisation with the `full` cost function, ID 4A (favouring `LLO_mu` over `LLO_sigma`), in the first 10 h of simulation.

In the plot 4 different quantities are displayed over the simulated timespan. The first row reports the DOP parameters, in particular `2DHDOP` (red dots) and `GDOP` (blue dots), indicating thus also the 3- and 4-fold visibility respectively. This is directly correlated with the second row of the plot, where the total number of servicers actually connected to the user is plotted over time. The third and the last rows indicate instead the estimation error on position and velocity respectively, expressed on a logarithmic scale.

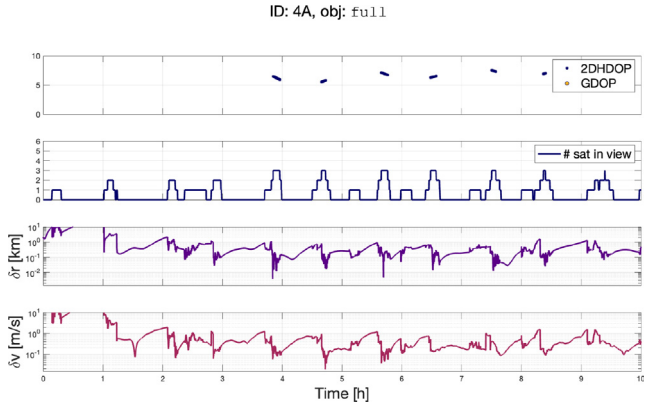

Fig. 7. Zoomed view of the first 10 h of navigation simulation outcomes for the $n = 4$ case of the `full` optimisation, ID 4A, minimising `LLO_mu`.

From these plots we can extract a clear trend, which is present in all the performed simulations for the whole 48 h. There is a continuous alternation of navigation availability and blind windows. During the former, the navigation solution converges rapidly to extremely good results, with errors in the order of 10m, practically consisting in the pseudorange measurement error. When the number of satellites in visibility is instead less than 3, the position error starts rising reaching quickly $\sim$ 100m and then drifting up to 1km and even higher in the worst cases.

We can see that optimising for good `2DHDOP` values (< 10 in this case) results in extremely good performance for position estimation. It is however still limiting the presence of blind windows. In such regions, the performance of state estimation is not always satisfactory, but remains bounded below 10km, after the starting convergence period.

In order to provide insight on the global navigation solutions, a recap of integral figures of merit is provided by Table 2, providing information on a subset of 8 solutions among the 16 extracted from the optimisations.

Among such indices we collected both δr_cum, δr_cumlkm and δv_cum which are the cumulative time in hours where the navigation errors overcome 100m, 1km and 10ms^{-1}. These last two values are considered as a possible threshold to define a navigation divergence, while the former defines good navigation performance. In addition to those we computed also $\mu_{\delta r}, \sigma_{\delta r}$ and $\max(\delta r)$, which are mean, standard deviation and maximum value recorded by the position error.

In the following, different side-by-side comparisons are proposed, in order to assess the capability of the optimisation procedure to address some specific points.

4.2.1. Cost function `full` vs `llo_sgl`

First of all, we compare what is obtained including or not the objectives associated to the South Pole surface user,

Table 2
Collection of navigation performance for a subset of the extracted optimal solutions, representing the different analysed cases and an LLO user with `ran`=0°.

Cost function	full		llo_sgl	llo_mlt
ID	4A	5A	5A	5A
δr_cum [h]	45.0	42.9	41.2	43.6
δr_cumlkm [h]	6.2	5.3	3.6	10.5
δv_cum [h]	0.82	0.40	0.01	0.04
$\mu_{\delta r}$ [km]	0.856	0.635	0.425	0.955
$\sigma_{\delta r}$ [km]	2.776	1.455	0.438	1.437
$\max(\delta r)$ [km]	41.2	34.9	9.1	7.6
Cost function		llo_sgl		
ID	4A	4B	6A	6B
δr_cum [h]	45.3	43.1	39.3	40.4
δr_cumlkm [h]	12.0	11.7	1.0	4.3
δv_cum [h]	0.05	0.29	0.067	0.076
$\mu_{\delta r}$ [km]	0.825	0.814	0.296	0.458
$\sigma_{\delta r}$ [km]	0.971	1.288	0.314	0.603
$\max(\delta r)$ [km]	9.6	18.2	10.8	13.2

thus looking at the `full` and `llo_sgl` cost functions. In particular, the cases for constellation sizes of $n = 4$ and $n = 5$ are taken into consideration, relating the results of Pareto points A in both cases. It is relevant to recall that for the `full` case (as in Fig. 7), solution A favours the average value of the maximum 2-fold blind windows, while for the `llo_sgl` one (as in Fig. 8), it is the product of mean and standard deviation of the same quantity that is prioritised.

By looking at the scores in Table 2, we see that for the $n = 4$ case, there are no major improvements from keeping only the `LLO` related objectives. Indeed the values obtained for δr_cum and $\mu_{\delta r}$ do not differ so much, while for the 1km threshold cumulative time, we have a practically doubled score. The only improving scores are found in the cumulative velocity threshold overcome and in the standard deviation of the position error, other than the maximum error experienced.

If we analyse instead the results of the $n = 5$ case we see that a major improvement overall is present. In particular, δv_cum is extremely reduced as well as $\sigma_{\delta r}$ and $\max(\delta r)$.

For both constellation sizes, the improvements are found principally in the position error standard deviation and maximum value. The former is the direct effect of including the Pareto solution comprising only the `LLO_mu` objective minimisation in the `full` cost function and not `LLO_sigma`, while in the second cost function the two objectives are already traded off, by minimising their product directly.

4.2.2. Objective `LLO_musigma` vs `LLO_cum`

The next comparison is performed by looking at results for solutions with ID A and those with ID B of the `llo_sgl` cost function. Recalling the Pareto points selection procedure for that specific optimisation results, we picked solutions minimising `LLO_musigma` (labelled with ID A) and others minimising `LLO_cum` (labelled with ID B). In this comparison we look at both $n = 4$ and $n = 6$,

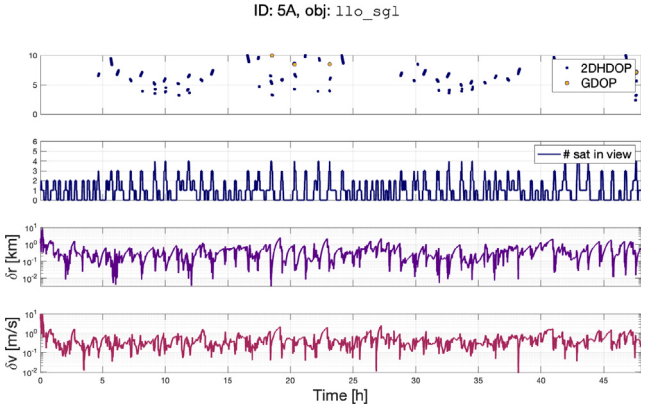

Fig. 8. Navigation simulation outcomes for the $n = 5$ case of the `llo_sgl` optimisation, ID 5A, Pareto knee point minimising both `LLO_musigma` and `LLO_cum`.

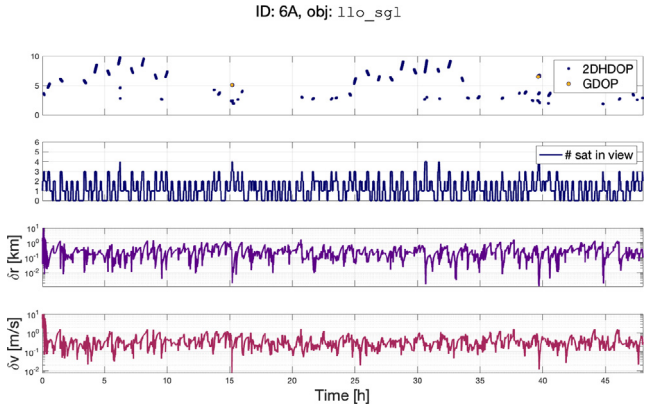

Fig. 9. Navigation simulation outcomes for the $n = 6$ case of the `llo_sgl` optimisation, ID 6A, Pareto optimal point minimising `LLO_musigma`.

so IDs 4A, 4B, 6A (see Fig. 9 and 6B (see Fig. 10), corresponding to the bottom part of Table 2.

In both the $n = 4$ and $n = 6$ cases we obtain comparable or slightly lower performance choosing solutions B over A. For the $n = 4$ case, the solution with `LLO_cum` presents slightly higher performance in the cumulative position errors and the average value. This is instead not the case for $n = 6$, where these parameters are worse in solution B. A deterioration of the performance is instead present in both sizes for the cumulative velocity error and for the position error standard deviation $\sigma_{\delta r}$ and maximum value $\max(\delta r)$.

Moreover, comparing the first row of Figs. 9 and 10 we can also see worse `GDOP` and `2DHDOP` values in the 6B case, although a general higher `2DHDOPAV` result is present, due to the specific objective favoured in its selection.

In general, the analysed cases show that no significant improvement can be achieved in the overall performance, by favouring the minimisation of 2-fold blind windows, with respect to the minimisation of the average and standard deviation values.

4.2.3. Cost function `llo_sgl` vs `llo_mlt`

All the previous solutions were obtained targeting a single value of `ran`, so specialised for a single class of polar LLO. The cost function `llo_mlt` has been set to provide performance to different orbital planes, with the goal of providing more reliable and robust solutions. The comparison we perform here is among the 5A solutions for the `llo_sgl` and `llo_mlt` cost functions, the former presented in Fig. 8, the latter in Fig. 11.

From the plots in Fig. 11 we can spot 2-3 h-long daily windows with a maximum of a single servicer satellite in visibility of the user. Indeed, recall that we are considering an LLO user with `ran` at 0°, serviced by a constellation optimised for a wider variety of users with `ran` $\in [0, 120, 240°]$. As such it is reasonable that some blind windows can be found.

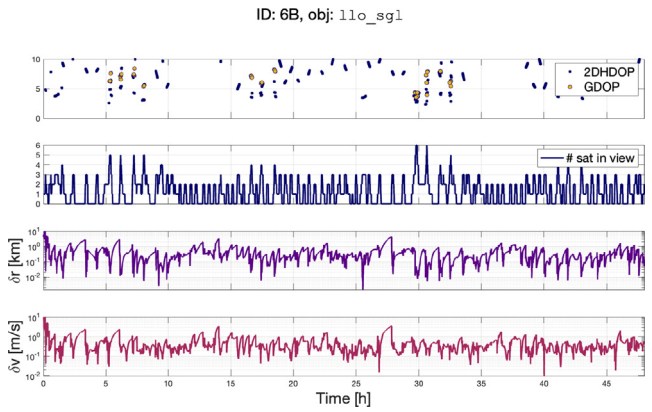

Fig. 10. Navigation simulation outcomes for the $n = 6$ case of the llo_sgl optimisation, ID 6B, Pareto optimal point minimising LLO_cum.

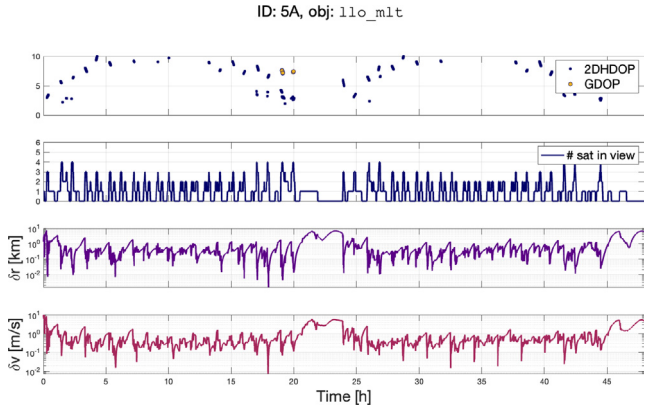

Fig. 11. Navigation simulation outcomes for the $n = 5$ case of the llo_mlt optimisation, ID 5A, Pareto optimal point minimising LLO_musigma.

This decrement in performance is also found by looking at Table 2, where the last two columns of the upper row provide a side-by-side comparison. Excluding max(δr), which is slightly better for the multi-plane optimised solution, we find a persistent performance degradation. E.g., the cumulative time spent with a position error higher than 1km is practically tripled, as well as the standard deviation of the error, indicating a more discontinuous and heterogeneous behaviour. In any case, a good remark about the llo_mlt cost function is that there are still parts of the day when good navigation performance is present, reaching position errors below 100m, giving the possibility to still perform most of the critical GNC tasks overall.

By looking instead at a different LLO user, placed on a plane with ran = 90°, we obtain the results in Table 3.

We can see here that for a user case for which the constellation was not optimised the two constellations perform similarly, with the multi-plane one, scoring worse in δr_cumlkm and in $\sigma_{\delta r}$. Looking at the comparison of these data per cost function with respect to the results for the user at ran=0°, we see an important decrement of performance for the llo_sgl cost function, while in the llo_mlt case we see a much more robust behaviour, keeping the performance more similar, fulfilling the rationale behind such a constellation optimisation choice.

Table 3
Collection of navigation performance for a subset of the extracted optimal solutions, representing the different analysed cases and an LLO user with ran = 90°.

Cost fcn	llo_sgl	llo_mlt
ID	5A	5A
δr_cum [h]	45.6	44.6
δr_cumlkm [h]	6.0	7.2
δv_cum [h]	0.16	0.16
$\mu_{\delta r}$ [km]	0.602	0.790
$\sigma_{\delta r}$ [km]	0.781	1.433
max(δr) [km]	11.7	11.8

4.2.4. Constellation size

The last analysis proposed here is to verify the improvements obtained in the llo_sgl cost function increasing the constellation size from 4 to 5 and finally to 6.

Overall we see a continuous improvement of the performance with the peak values obtained in the 6A case. The only two parameters not following strictly the increment are the cumulative time with velocity error above 10ms^{-1} and the maximum position error. In both situations the best score is obtained with the 5A case. If the maximum value encountered in the position error is something that levels out after the transient completion and thus not deemed as a fundamental parameter, the worse score in the velocity error parameter can be explained likely by the higher eccentricity found in the 5A case, e = 0.583, with respect to the 6A case, e = 0.489. The higher value provides larger servicer velocity value excursions, thus a higher measured *range-rate* excursion, which increases the observability of the velocity itself.

5. Conclusions

This paper presented a complete framework for supporting the preliminary phase design of a satellite constellation to provide communication and navigation services to both South Pole and Low Lunar Orbit users. However, it may not be the optimal approach if one targets a full global coverage or has loose constraints on the number of servicing satellites, in which case a traditional GNSS-like constellation geometry would provide better performance. The developed system is capable to provide the flexibility requested by such early stages of the mission analysis, where the overall requirements are not completely defining a specific performance index. In such cases, exploiting MOO is a good choice to combine different objectives which may be clashing among themselves or may be uninfluenced. Moreover, such multi-objective scheme outputs a whole population of solutions, a subset of which represents usually a Pareto front, from which we can understand the

boundaries of feasibility and then pick the solutions that fit our needs the most.

The optimisation has been exploited to cast together objectives associated to either the surface users or the LLO ones. In particular three different cost functions are taken into consideration with or without the South Pole related objectives, each one run for three different constellation sizes. The resulting populations of solutions have been inspected through various Pareto plots and a total of 16 possible candidates are extracted with optimal related performance.

A subset of these candidates then has been analysed in terms of the navigation performance, when simulated with an LLO polar user at an altitude of 50km at `ran` values of 0 and 90°. The navigation filter employed here considers a tightly coupled GNSS/INS formulation, where the servicers pseudorange and pseudorange-rate measurements are fused to the ones of an accelerometer. The presented architecture provided an alternating behaviour of regions with extremely good performance in state reconstruction and regions of loss of GNSS support, where the accelerometer inertial navigation starts loosing accuracy leading in some cases to acceptable levels ($<$ 1km) and unacceptable in some others ($>$ 10km). The comparison of the obtained navigation filter results correlated to cost function and constellation size provides some useful insights, such as the increment in performance looking at the minimisation of the combined position error average and standard deviation values, `LLO_musigma` against the minimisation of cumulative 2-fold blind windows. Moreover the robustness of optimising for a wide variety of LLO users orbital plane has been proved, by comparing the `llo_sgl` with `llo_mlt` cost functions. In the latter, even though lower performance are obtained in general for the optimised orbital planes, a higher resilience of the results is present when looking at non-optimised solutions for orbital planes.

Future works may also investigate some mitigating strategy for the sensor fusion architecture, in order to increment the accuracy of state reconstruction during the blind windows, for example, by including also an altimeter in the sensor suite. Moreover, adding a more refined model of the accelerometer, which includes also bias and drift, may increase the fidelity of the overall system. In this situation the navigation filter may also be used for the accelerometer bias and drift estimation.

Declaration of Competing Interest

The authors declare that they have no known competing financial interests or personal relationships that could have appeared to influence the work reported in this paper.

References

Acciarini Giacomo, Izzo Dario, Mooij Erwin, 2020. MHACO: a multi-objective hypervolume-based ant colony optimizer for space trajectory optimization. In: 2020 IEEE Congress on Evolutionary Computation (CEC), pp. 1–8, https://doi.org/10.1109/CEC48606.2020.9185694.

Acton Jr., Charles H., 1996. Ancillary data services of NASA's navigation and ancillary information facility. Planet. Space Sci. 44 (1), 65–70.

Biscani, Francesco, Izzo, Dario, 2020. A parallel global multiobjective framework for optimization: pagmo. J. Open Source Softw. 5 (53), 2338. https://doi.org/10.21105/joss.02338, URL https://doi.org/10.21105/joss.02338.

Capannolo, Andrea, Lavagna, Michèle, 2022. Adaptive state-dependent riccati equation control for formation reconfiguration in cislunar space. J. Guidance Control Dyn. 45 (5), 982–989.

Capannolo, Andrea, Zanotti, Giovanni, Lavagna, Michèle, Cataldo, Giuseppe, 2023. Model predictive control for formation reconfiguration exploiting quasi-periodic tori in the cislunar environment. Nonlinear Dyn., 1–19 https://doi.org/10.1007/s11071-022-08214-8.

Ceresoli Michele, Zanotti Giovanni, Lavagna Michèle, 2021. Bearing-only navigation for proximity operations on cis-lunar non-keplerian orbits. In: 72nd International Astronautical Congress (IAC 2021), pp. 1–10.

Colagrossi Andrea, Pesce Vincenzo, Bucci Lorenzo, Colombi Francesco, Lavagna Michèle, 2021. Guidance, navigation and control for 6dof rendezvous in cislunar multi-body environment. Aerospace Sci. Technol. 114:106751, 2021. ISSN 1270-9638. https://doi.org/10.1016/j.ast.2021.106751. https://www.sciencedirect.com/science/article/pii/S1270963821002613.

Crassidis, John L., Junkins, John L., 2011. Optimal Estimation of Dynamic Systems. CRC Press.

Curtis, Howard, 2013. Orbital mechanics for Engineering Students. Butterworth-Heinemann.

Deb, Kalyanmoy, Pratap, Amrit, Agarwal, Sameer, Meyarivan, T.A.M. T., 2002. A fast and elitist multiobjective genetic algorithm: NSGA-II. IEEE Tran. Evol. Comput. 6 (2), 182–197.

ESA, 2021. Moonlight: connecting Earth with the Moon, https://www.esa.int/ESA_Multimedia/Videos/2021/05/Moonlight_bringing_connectivity_to_the_Moon.

European Commission, 2019. European GNSS (Galileo) Open Service - Service Definition Document (SDD).

Falco, Gianluca, Pini, Marco, Marucco, Gianluca, 2017. Loose and tight GNSS/INS integrations: Comparison of performance assessed in real urban scenarios. Sensors 17 (2), 255.

Giordano Pietro, Grenier Antoine, Zoccarato Paolo, Bucci Lorenzo, Cropp Alexander, Swinden Richard, Gomez Otero, D., El-Dali Wael, Carey William, Duvet Ludovic, et al., 2021. Moonlight navigation service-how to land on peaks of eternal light. In: Proceedings of the 72nd International Astronautical Congress (IAC), Dubai, United Arab Emirates, pp. 25–29.

Grenier, Antoine, Giordano, Pietro, Bucci, Lorenzo, Cropp, Alexander, Zoccarato, Paolo, Swinden, Richard, Ventura-Traveset, Javier, 2022. Positioning and velocity performance levels for a Lunar Lander using a dedicated Lunar Communication and Navigation System. NAVIGATION: J. Inst. Navigat. 69 (2).

International Space Exploration Coordination Group (ISECG), 2019. Global Exploration Roadmap Critical Technology Needs.

Israel, David J., Mauldin, Kendall D., Roberts, Christopher J., Mitchell, Jason W., Pulkkinen, Antti A., Cooper La Vida, D., Johnson, Michael A., Christe, Steven D., Gramling, Cheryl J., 2020. Lunanet: a flexible and extensible lunar exploration communications and navigation infrastructure. In: 2020 IEEE Aerospace Conference. IEEE, pp. 1–14.

Jessica Flahaut, J., Carpenter, J-P Williams, Anand, M., Crawford, I.A., van Westrenen, W., Füri, E., Xiao, L., Zhao, S., 2020. Regions of interest (ROI) for future exploration missions to the lunar south pole. Planet. Space Sci. 180, 104750.

Kaplan, Elliott D., 2017. Christopher Hegarty, Understanding GPS/GNSS: principles and applications. Artech House.

Konopliv, A.S., Binder, A.B., Hood, L.L., Kucinskas, A.B., Sjogren, W. L., Williams, J.G., 1998. Improved gravity field of the moon from lunar prospector. Science 281 (5382), 1476–1480. https://doi.org/10.1126/science.281.5382.1476.

Laurini, Kathleen C., Hufenbach Bernhard, Kawaguchi Junichiro, Piedbœuf Jean-Claude, Schade Britta, Curtis Jeremy, Kim, H., 2010. An international strategy for human exploration of the moon: the international space exploration coordination group (ISECG) reference architecture for human lunar exploration. In: Proceedings of the 61st International Astronautical Congress, International Astronautical Federation (IAF) Paris, pp. 1–9.

Li Xiaodong, 2003. A non-dominated sorting particle swarm optimizer for multiobjective optimization. In: Genetic and Evolutionary Computation — GECCO 2003, Berlin, Heidelberg. Springer, Berlin Heidelberg, pp. 37–48. ISBN 978-3-540-45105-1.

Lunghi Paolo, Di Lizia Pierluigi, Armellin Roberto, Lavagna Michèle, 2022. Semi-analytical adaptive guidance computation for autonomous planetary landing. Acta Astronaut, 195,265–275. ISSN 0094-5765. https://doi.org/10.1016/j.actaastro.2022.03.005. https://www.sciencedirect.com/science/article/pii/S0094576522001035.

Northrop Grumman, 2022. LN-200S Inertial Measurement Unit Datasheet.

Pasquale, A., Zanotti, G., Prinetto, J., Ceresoli, M., Lavagna, M., 2022a. Cislunar distributed architectures for communication and navigation services of lunar assets. Acta Astronaut. 199, 345–354. https://doi.org/10.1016/j.actaastro.2022.06.004, ISSN 0094-5765..

Pasquale, Andrea, Silvestrini, Stefano, Capannolo, Andrea, Lunghi, Paolo, Lavagna, Michèle, 2022b. Small bodies non-uniform gravity field on-board learning through hopfield neural networks. Planet. Space Sci., 105425

Schaub, Hanspeter, Junkins, John L., 2005. Analytical Mechanics of Space Systems. American Institute of Aeronautics and Astronautics.

Silvestrini, Stefano, Piccinin, Margherita, Zanotti, Giovanni, Brandonisio, Andrea, Bloise, Ilaria, Feruglio, Lorenzo, Lunghi, Paolo, Lavagna, Michèle, Varile, Mattia, 2022a. Optical navigation for lunar landing based on convolutional neural network crater detector. Aerosp. Sci. Technol. 123, 107503.

Silvestrini Stefano, Piccinin Margherita, Zanotti Giovanni, Brandonisio Andrea, Lunghi Paolo, Lavagna Michèle, 2002b. Implicit extended kalman filter for optical terrain relative navigation using delayed measurements. Aerospace, 9(9), ISSN 2226-4310. https://doi.org/10.3390/aerospace9090503. https://www.mdpi.com/2226-4310/9/9/503.

Stadler Wolfram, 1988. Multicriteria Optimization in Engineering and in the Sciences, vol. 37. Springer Science & Business Media.

Vallado, David A., 2001. Fundamentals of astrodynamics and applications, vol. 12. Springer Science & Business Media.

Wilhelms, Don E., Howard, Keith A., Gordon Wilshire Howard, 1979. Geologic map of the south side of the Moon. Department of the Interior, US Geological Survey.